


Cite this: *RSC Adv.*, 2023, 13, 22335

# Fluorinated hydrogel nanoparticles with regulable fluorine contents and $T_2$ relaxation times as $^{19}\text{F}$ MRI contrast agents†

Ziwei Duan,<sup>a</sup> Changjiang Liu,<sup>a</sup> Junjie Tang,<sup>a</sup> Ruling Zhang,<sup>a</sup> Danfeng Peng,<sup>b</sup> Ruitao Lu,<sup>b</sup> Zong Cao<sup>\*a</sup> and Dalin Wu<sup>id</sup> <sup>\*a</sup>

Medical imaging contrast agents that are able to provide detailed biological information have attracted increasing attention. Among the new emerging imaging contrast agents,  $^{19}\text{F}$  magnetic resonance imaging contrast agents ( $^{19}\text{F}$  MRI CAs) are extremely promising for their weak background disturbing signal from the body. However, to prepare  $^{19}\text{F}$  MRI CAs with a long  $T_2$  relaxation time and excellent biocompatibility in a simple and highly effective strategy is still a challenge. Herein, we report a new type of  $^{19}\text{F}$  MRI hydrogel nanocontrast agents ( $^{19}\text{F}$  MRI HNCAs) synthesized by a surfactant-free emulsion polymerization with commercial fluorinated monomers. The  $T_2$  relaxation time of  $^{19}\text{F}$  MRI HNCA-1 was found to be 25–40 ms, guaranteeing its good imaging ability *in vitro*. In addition, according to an investigation into the relationship between the fluorine content and  $^{19}\text{F}$  MRI signal intensity, the  $^{19}\text{F}$  MRI signal intensity was not only determined by the fluorine content in  $^{19}\text{F}$  MRI HNCAs but also by the hydration microenvironment around the fluorine atoms. Moreover,  $^{19}\text{F}$  MRI HNCAs demonstrated excellent biocompatibility and imaging capability inside cells. The primary exploration demonstrated that  $^{19}\text{F}$  MRI HNCAs as a new type of  $^{19}\text{F}$  MRI contrast agent hold potential for imaging lesion sites and tracking cells *in vivo* by  $^{19}\text{F}$  MRI technology.

Received 29th April 2023

Accepted 10th July 2023

DOI: 10.1039/d3ra02827e

rsc.li/rsc-advances

## Introduction

Magnetic resonance imaging (MRI) has gained increasing attention in modern medical diagnosis, because it can allow collecting high-quality information of soft tissues without the use of harmful radioactive nuclides.<sup>1–3</sup> Traditionally, MRI technology depends on the local differences in proton spin densities and the relaxation rates of water protons *in vivo*. However, the above-mentioned two parameters do not have significant differences between detecting sites and healthy tissues in the body, resulting in a failure to obtain sufficient contrast or provide precise information. As a result, contrast agents (CAs) are normally introduced in MRI examination to enhance the image contrast by regulating the relaxation properties of the neighboring water protons.<sup>4,5</sup> At present, the normally introduced  $^1\text{H}$  MRI CAs in clinical use are paramagnetic and superparamagnetic meta ion-based species, such as gadolinium chelates and iron oxide nanoparticles.<sup>6,7</sup> Although a significant enhancement of MRI performance by applying

paramagnetic and superparamagnetic meta ion-based compounds has been achieved, the  $^1\text{H}$  MRI CAs still possess some limitations, especially their application security,<sup>8</sup> which should be seriously considered. For example, gadolinium-based CAs are able to cause nephrogenic systemic fibrosis in patients with impaired kidney function according to a recent symmetrically study.<sup>9,10</sup>

To further improve the safety of MRI, researchers have started to develop other types of MRI CAs based on heteronuclear atoms, such as fluorine.<sup>11,12</sup> Different from  $^1\text{H}$  MRI CAs that influence the relaxation properties of nearby water protons, the fluorine atoms in  $^{19}\text{F}$  MRI CAs are able to be visualized directly by MRI equipment.<sup>13</sup> In addition,  $^{19}\text{F}$  has a 100% natural abundance and a gyromagnetic ratio close to hydrogen (83% compared with hydrogen), giving  $^{19}\text{F}$  MRI excellent imaging resolution.<sup>14</sup> Another advantage of  $^{19}\text{F}$  MRI is the images have a higher imaging contrast due to the absence of  $^{19}\text{F}$  atoms in the detecting domains.<sup>15</sup> In addition, the signal intensity in  $^{19}\text{F}$  MRI is proportional to the fluorine content, enabling the quantitative application of  $^{19}\text{F}$  MRI.<sup>16</sup>  $^{19}\text{F}$  MRI is able to provide more insightful information of soft tissues *in vivo* over  $^1\text{H}$  MRI since the fluorine atoms *in vivo* are mainly embedded in the solid matrices of teeth and bones *in vivo*.<sup>17</sup> In principle, any species containing fluorine atoms, including small molecules,<sup>18,19</sup> macromolecules,<sup>20</sup> and nano-objectives,<sup>21</sup> has potential as  $^{19}\text{F}$  MRI CAs.

<sup>a</sup>School of Biomedical Engineering, Shenzhen Campus of Sun Yat-Sen University, Shenzhen, 518107, China. E-mail: wudlin6@mail.sysu.edu.cn; caozhong@mail.sysu.edu.cn

<sup>b</sup>Shenzhen International Institute for Biomedical Research, Shenzhen, 518109, China

† Electronic supplementary information (ESI) available. See DOI: <https://doi.org/10.1039/d3ra02827e>


Perfluorocarbons (PFCs), because of their high fluorine content, have been widely investigated as  $^{19}\text{F}$  MRI CAs.<sup>22</sup> In practice, PFCs are not the best molecules as  $^{19}\text{F}$  MRI CAs, because of their serious accumulation in the liver and spleen.<sup>23,24</sup> In addition, the low boiling point of PFCs prohibits this type of  $^{19}\text{F}$  MRI CAs from achieving long-term storage *in vitro* and circulation *in vivo*, even though the PFC emulsions are stabilized by robust surfactants.<sup>25,26</sup> The fluorine content in  $^{19}\text{F}$  MRI CAs is not the only parameter determining the imaging result of  $^{19}\text{F}$  MRI CAs. For high-efficiency  $^{19}\text{F}$  MRI CAs, fluorine atoms should hold very excellent local mobility in  $^{19}\text{F}$  MRI CAs under hydration condition, which can ensure a  $T_2$  relaxation time of  $^{19}\text{F}$  MRI CAs above 10 ms to guarantee sufficient signal collecting intensity during measurement.<sup>27</sup> It is well known that the strong hydrophobicity of fluorine atoms causes them to aggregate in  $^{19}\text{F}$  MRI CAs, further lose their local mobility, and shorten the  $T_2$  relaxation time under hydration conditions.<sup>28</sup> In order to solve this critical problem, various strategies have been explored by researchers, such as copolymerizing fluorine-based monomers with various hydrophilic monomers to create a hydration environment around fluorine atoms,<sup>29,30</sup> synthesizing hydrophilic monomers appending fluorine atoms,<sup>31</sup> and developing smart “On-Off” signal amplifying  $^{19}\text{F}$  MRI CAs echoing physiological triggers.<sup>32,33</sup> Changkui Fu *et al.* recently reported water-soluble fluoropolymers with sulfoxide side-chains as low-fouling  $^{19}\text{F}$  MRI CAs ( $T_2 = 373\text{--}431$  ms). Their results demonstrated that introducing water-soluble groups around fluorine atoms in  $^{19}\text{F}$  MRI CAs is an impactful strategy to prolong the  $T_2$  relaxation time and enhance the imaging efficacy *in vitro* and *in vivo*.<sup>34</sup> More directly, Jinhao Gao *et al.* applied water-soluble fluorine-containing ionic liquids ( $T_2 = 4.4$  s) as fluorine markers in  $^{19}\text{F}$  MRI. They encapsulated a fluorine-containing ionic liquid inside porous silica nanoparticles and the ionic liquids were sealed by pH-responsive polymers on the surface of the porous silica nanoparticles. Their hybrid system acted as a pH-responsive “Off-On”  $^{19}\text{F}$  MRI CA.<sup>35</sup> Apart from the mobility of fluorine atoms in the  $^{19}\text{F}$  MRI CAs, the magnetically equivalency of the fluorine nuclei is another determinative factor in the  $^{19}\text{F}$  MRI CAs performance, because un-equivalent fluorine nuclei can result in blurry MR images.<sup>36</sup>

In order to achieve high performance in  $^{19}\text{F}$  MRI, the influence of the topological structures (linear, block, hyperbranched, star-like) and nanostructures (micelles, vesicles, and worm-like micelles) of  $^{19}\text{F}$  MRI CAs on the imaging performance have also been explored in depth,<sup>37–43</sup> because the mobility of the fluorine atoms in  $^{19}\text{F}$  MRI CAs is determined by the topological structures, while the uptake and accumulation behavior of the  $^{19}\text{F}$  MRI CAs inside disease lesions are influenced by their nanostructures.<sup>44,45</sup> For example, Kristofer J. Thurecht *et al.* explored the influence of the topology structure on the  $T_2$  relaxation times and imaging performance of  $^{19}\text{F}$  MRI CAs by synthesizing a series of hyperbranched polymeric scaffolds. The longest  $T_2$  relaxation time of 71 ms could be obtained by incorporating hydrophilic oligo(ethyl glycol) ( $M_w = 400$ ) in their hyperbranched  $^{19}\text{F}$  MRI CAs.<sup>29</sup> In the last two decades, polymerization-induced self-assembly (PISA) as a heterogeneous polymerization technology has been developed as an

extraordinary powerful method to fabricate different nanostructures of amphiphiles, and accordingly, PISA has been also received increasing attention in  $^{19}\text{F}$  MRI CAs preparation. Wei Zhao *et al.* first prepared poly(oligo(ethylene glycol) methyl ether acrylate-co-2,2,2-trifluoroethyl acrylate) (poly(OEGA-co-TFEA)) as a macro-RAFT chain transferring agent (macro-CTA). After that, AIBN initiated the PISA of styrene and 3-vinyl benzaldehyde with macro-CTA in isopropanol to form  $^{19}\text{F}$  MRI CAs with micelles, worm-like micelles, and polymersomes nanostructures. The results revealed that the  $^{19}\text{F}$  MRI CAs with a worm-like nanostructure had the best cell-uptake behavior compared with the others. The  $T_2$  relaxation times of all the  $^{19}\text{F}$  MRI CAs were from 176 ms to 179 ms in  $\text{D}_2\text{O}$ . This work indicated the great potential of utilizing PISA to prepare  $^{19}\text{F}$  MRI CAs and to adjust their morphologies.<sup>46</sup>

The imaging performance of the newly synthesized  $^{19}\text{F}$  MRI CAs have been improved considerably in the last two decades. However, most of the high-performance  $^{19}\text{F}$  MRI CAs developed to date require many synthetic steps and tedious purification procedures in their preparation process, which prohibits most of the synthesized  $^{19}\text{F}$  MRI CAs from practical application in clinical use. Thus, exploring facile strategies to fabricate high-performance  $^{19}\text{F}$  MRI CAs with acceptable preparation procedures still requires attention and effort. Some research has revealed that to achieve high-resolution *in vivo*  $^{19}\text{F}$  MRI, a very high concentration of  $^{19}\text{F}$  MRI CAs (above 50 mM) is normally administrated,<sup>47–49</sup> which indicates that prolonging the circulation time of the  $^{19}\text{F}$  MRI CAs in vessels *in vivo* and promoting their accumulation inside the imaging lesion *in vivo* are pivotal as well. Thus, fabricating high-performance  $^{19}\text{F}$  MRI CAs with a long  $T_2$  relaxation time and long circulation time *in vivo* and with excellent biocompatibility by a simple, efficient, and economical strategy demands increasing attention from researchers.

Herein, we present a new type of  $^{19}\text{F}$  MRI hydrogel nanoparticle contrast agents ( $^{19}\text{F}$  MRI HNCAs) synthesized by a surfactant-free emulsion polymerization of the commercial fluorinated monomers (Fig. 1). We hypothesize that the hydration state in hydrogel nanoparticles is able to render the fluorine atoms with enough mobility, allowing the  $T_2$  relaxation times of the  $^{19}\text{F}$  MRI HNCAs to be over 10 ms. Our explorations demonstrated a  $T_2$  relaxation time of the  $^{19}\text{F}$  MRI HNCAs of 25–40 ms at concentrations ranging from 5–40  $\text{mg mL}^{-1}$  under a magnetic field strength of 9.4 T. They displayed excellent  $^{19}\text{F}$  NMR intensity in  $\text{D}_2\text{O}/\text{H}_2\text{O}$  (1/9, v/v) and were able to image well *in vitro*. In addition, the  $^{19}\text{F}$  MRI HNCAs demonstrated excellent biocompatibility and great colloid stability in aqueous solution (PBS buffer) for more than one year at room temperature. Most essentially, we found that the  $^{19}\text{F}$  NMR intensity and imaging efficiency mainly depended on the mobility of fluorine atoms rather than the fluorine content inside the  $^{19}\text{F}$  MRI HNCAs. Increasing the fluorine content in the  $^{19}\text{F}$  MRI HNCA blindly without considering the mobility of the fluorine atoms resulted in an attenuation of the  $^{19}\text{F}$  NMR signal intensity and imaging capability. The present research results have great significance in the design and preparation of other advanced  $^{19}\text{F}$  MRI CAs.



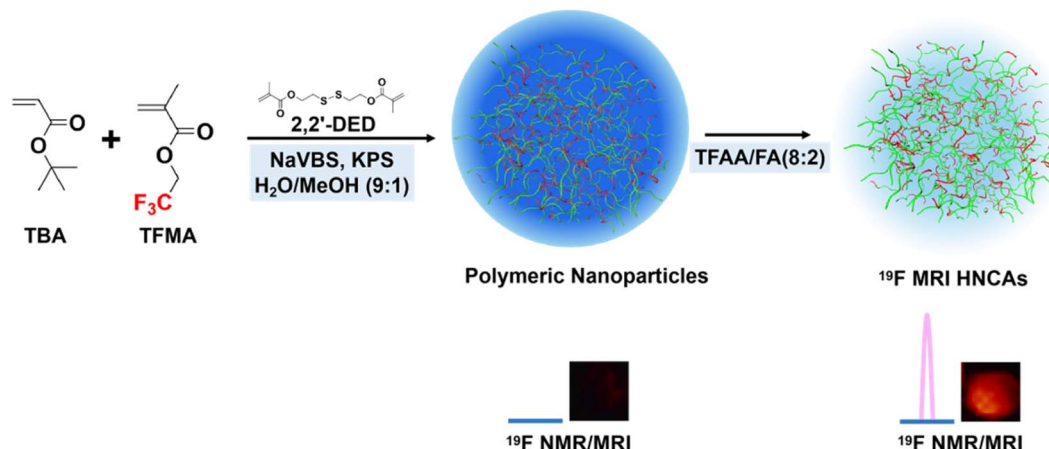


Fig. 1 Schematic illustration of the synthesis process and constitution of the  $^{19}\text{F}$  MRI HNCAs.

## Experimental section

### Materials

Methacryloyl chloride (MAC) (95%), 2,2,2-trifluoroethyl methacrylate (98%), tertiary-butyl acrylate (TBA) (99%), 2,2,2-trifluoroethyl methacrylate (TFMA) (98%), sodium 4-vinylbenzenesulfonate (NaVBS) (90%), potassium persulfate (KPS) (99.9%), trifluoroacetic acid (TFAA) (99%), and *n*-hydroxysuccinimide (NHS) (95%) were purchased from Shanghai Acme Biochemical. Bis-(2-hydroxyethyl) disulfide (BHDSH) (>90%) was a product of Shanghai Aladdin Biochemical Technology. Triethylamine (99.5%), methanol ( $\geq 99.9\%$ ), 3,6-diamino-9-[2-(methoxycarbonyl)phenyl]-xanthylum chloride (Rhodamine-123) (98%), and 1-ethyl-3-(3-dimethylaminopropyl) carbodiimide hydrochloride (EDC·HCL) ( $\geq 97\%$ ) were products of Anhui Senrise Technology. Deuterium oxide ( $\text{D}_2\text{O}$ ) (99.9%) and chloroform- $d$  ( $\text{CDCl}_3$ ) (99.8%) were purchased from Shanghai Macklin Biochemical Technology. Dichloromethane (DCM) ( $\geq 98\%$ ), formic acid (FA) ( $\geq 88\%$ ), ethyl acetate (EA) (99.5%), and petroleum ether (PE) ( $\geq 99.9\%$ ) were purchased from Guangzhou Brand. Dimethyl sulfoxide (DMSO) (99.9%) was obtained from Beijing Innochem Technology. Tertiary-butyl acrylate and 2,2,2-trifluoroethyl methacrylate were passed through  $\text{Al}_2\text{O}_3$  to remove the stabilizer before usage. Phosphotungstate negative staining solution (PNSS) (2%, pH 7.0) was purchased from Leagene Biotechnology. Dulbecco's modified eagle medium (DMEM) with 4.5 g  $\text{L}^{-1}$  D-glucose, L-glutamine, 110 mg  $\text{mL}^{-1}$  sodium, fetal bovine serum (FBS), and antibiotic-antimycotic (AA) were purchased from Thermo Fisher Scientific. Phosphate-buffered saline (PBS) was purchased from Beijing Solarbio Science & Technology. 3-(4,5-Dimethylthiazol-2-yl)-2,5-diphenyltetrazolium bromide (MTT) was purchased from Shanghai Aladdin Biochemical Technology. DAPI staining solution (DAPI) (98%) (2  $\mu\text{g mL}^{-1}$ ) was a product of Wuhan Servicebio Technology. Paraformaldehyde (PFA) was purchased from biosharp.

### Synthesis of disulfide dimethacrylate (2,2'-DED)

2,2'-DED was synthesized according to the literature.<sup>50</sup> BHDSH (1.5425 g, 10 mmol) and triethylamine (4.1699 mL, 30 mmol)

were dissolved in DCM (30 mL) in a two-necked flask equipped with argon (Ar). After the mixture was cooled down by immersion in an ice bath, MAC (2.6135 g, 25 mmol) was added dropwise. The reaction continued under an Ar atmosphere at room temperature for 24 h. The reaction was extracted by DCM and washed with water and brine, dried, and concentrated under vacuum. The crude product was purified by silica gel column chromatography (EA : PE = 1 : 15) to give a lightly yellow colored liquid 1.8920 g (72% yield).  $^1\text{H}$  NMR ( $\text{CDCl}_3$ , 400 MHz, ppm): 6.13 (2H, s, 2H), 5.59 (2H, q, 2H), 4.41 (4H, t, 4H), 2.98 (4H, t, 4H), 1.94 (6H, s, 6H). The NMR spectra was provided in the ESI (Fig. S6 $^\dagger$ ).

### Synthesis of $^{19}\text{F}$ MRI HNCAs-1

The polymeric nanoparticles (PNs) were synthesized by a surfactant-free emulsion polymerization. NaVBS (40 mg) and KPS (20 mg) were dissolved in a 40 mL mixture of  $\text{H}_2\text{O}$  and methanol (90/10, v/v). TBA, TFMA, and 2,2'-DED were then added into above solution. Then, oxygen was removed by bubbling argon through the solution for 20 min. The polymerization was carried out under an argon atmosphere at 70  $^\circ\text{C}$  for 18 h. The produced PNs were washed three times with ethanol and finally with  $\text{H}_2\text{O}$ .  $^{19}\text{F}$  MRI HNCAs-1 were finally prepared by hydrolyzing the *tert*-butyl groups of the PNs in a mixture of TFAA and FA (80/20, v/v). The product was finally dialyzed against  $\text{ddH}_2\text{O}$  for 48 h with changing the  $\text{ddH}_2\text{O}$  three times.

### Synthesis of rhodamine-123 modified $^{19}\text{F}$ MRI HNCAs-1 ( $^{19}\text{F}$ MRI HNCAs-1 Rh-123)

$^{19}\text{F}$  MRI HNCAs-1 (100 mg) were first dispersed in anhydrous DMSO (2 mL) in a two-necked flask under an argon atmosphere. Then, EDC·HCL (1 mg, 0.005216 mmol) and NHS (600  $\mu\text{g}$ , 0.005214 mmol) were added into the above DMSO solution. The flask was immersed in an ice bath. After 30 min, rhodamine-123 (200  $\mu\text{g}$ , 0.0005252 mmol) was added. The mixture was allowed to react at room temperature in the dark for 36 h. The rhodamine-123 modified  $^{19}\text{F}$  MRI HNCAs-1 were washed three times with ethanol and finally with DMSO. The obtained  $^{19}\text{F}$

MRI HNCAs-1 Rh-123 were dispersed in DMSO and stored in the refrigerator at  $-4\text{ }^{\circ}\text{C}$ .

### Transmission electron microscopy (TEM) analysis

TEM measurements were carried out using an HT7800 SEM instrument (Hitachi High-Tech Scientific Solutions, Japan). The operating pressure of electricity was set to 120 kV. The sample was stained by PNSS as a contrast agent before the measurements.

### Dynamic light scattering (DLS) and zeta potential measurements

DLS and zeta potential measurements were carried out using a Zetasizer Nano-ZS90 instrument (Malvern Instruments, Malvern, U.K.) equipped with a 4.0 mV He-Ne laser operating at 633 nm and a detection angle of  $173^{\circ}$ . The measuring temperature was set as  $25\text{ }^{\circ}\text{C}$ . The number-weighted hydrodynamic diameter was obtained from analysis of the autocorrelation functions using the method of cumulants. Three measurements were made for each sample with 60 s equilibrium time before each measurement. The concentration of the objectives was  $5\text{ mg mL}^{-1}$  in PBS.

### $^{19}\text{F}$ Nuclear magnetic resonance ( $^{19}\text{F}$ NMR)

$^{19}\text{F}$  NMR experiments were carried out on a Bruker AVANCE III HD Ascend 400 MHz spectrometer using a 12  $\mu\text{s}$  pulse width, relaxation delay of 1 s, acquisition time of 0.72 s, and 32 scans at  $25\text{ }^{\circ}\text{C}$ . All the chemical shifts are given herein in ppm.

### Spin-lattice relaxation times ( $T_1$ )

The  $T_1$  times were measured on a Bruker AVANCE III HD Ascend 400 MHz spectrometer using the standard inversion-recovery pulse sequence at  $25\text{ }^{\circ}\text{C}$ . The samples were dissolved in a mixture of  $\text{D}_2\text{O}/\text{PBS}$  (10/90, v/v) with a certain concentration. For each measurement, the relaxation delay was 1 s and the number of scans was 8.

### Spin-spin relaxation times ( $T_2$ )

The  $T_2$  times of the  $^{19}\text{F}$  HNCAs were measured using the Carr-Purcell-Meiboom-Gill (CPMG) pulse sequence at  $25\text{ }^{\circ}\text{C}$ . The  $^{19}\text{F}$  MRI HNCAs were dispersed in a mixture of  $\text{D}_2\text{O}/\text{PBS}$  (10/90, v/v) with a certain concentration. The relaxation delay was 2 s, and the number of scans was 32. For each measurement, the echo times were set from 10 to 1200 s, and 14 points were collected. The decay in amplitude of the spin echo could be described by a single-exponential function, which allowed calculating the  $T_2$  relaxation times.

### $^{19}\text{F}$ MRI imaging

Images of phantoms containing the  $^{19}\text{F}$  MRI HNCAs solutions were acquired on a Bruker BioSpec 94/20 USR MRI at 9.4 T. The  $^{19}\text{F}$  MRI HNCAs solutions (concentrations from  $0\text{ mg mL}^{-1}$  to  $40\text{ mg mL}^{-1}$  in PBS) were loaded in 2 mL Schering bottles.  $^1\text{H}$  MRI images were acquired using the RARE sequence (field of view = 4 cm, slice thickness = 20 mm,  $T_E = 8.5\text{ ms}$ ,  $T_R = 1000$

ms, number of averages = 32, FOV =  $40 \times 40\text{ mm}^2$ , matrix =  $32 \times 32$ ).  $^{19}\text{F}$  MRI images were acquired using the FLASH sequence (field of view = 4 cm, slice thickness = 20 mm,  $T_E = 1.3\text{ ms}$ ,  $T_R = 800\text{ ms}$ , number of averages = 32, FOV =  $40 \times 40\text{ mm}^2$ , matrix =  $32 \times 32$ ).

### Cytotoxicity studies

To quantify a potential impact on cell viability, the MTT assay was applied. Cells were cultured with  $^{19}\text{F}$  MRI HNCAs (concentrations from  $0\text{ mg mL}^{-1}$  to  $10\text{ mg mL}^{-1}$ ) in a 96-well plate in a final volume of 200  $\mu\text{L}$  for 24 h. The MTT solution (20  $\mu\text{L}$ ) was added into each well and incubated for 4 h. The liquid in each well of the plate was suction removed, and washed with PBS once. The DMSO (150  $\mu\text{L}$ ) was added into each well of the plate, and subsequently incubated on a shaker for 5 min. Finally, the absorbance of the cells was measured using a multifunctional microplate detector (BioTek Instrument, U.S.) at 490 nm.

### Confocal microscopy analysis

Imaging was conducted to identify if the  $^{19}\text{F}$  MRI HNCAs-1 were internalized by the cells. Cells were seeded at a density of 100 000 cells per dish onto a confocal dish. Next,  $5\text{ mg mL}^{-1}$  rhodamine-123 modified  $^{19}\text{F}$  MRI HNCAs were added and incubated for 4 h. The cells were fixed for 15 min in 4% PFA, before being rinsed for  $3 \times 5\text{ min}$  in PBS. Subsequently, DAPI was added to the fixed cells and incubated for 10 min, before being rinsed for  $3 \times 5\text{ min}$  in PBS. Images were acquired using an Olympus FV3000 laser confocal microscope and were analyzed using XV Viewer software.

### Biosafety

The biosafety of the  $^{19}\text{F}$  MRI HNCAs-1 was assessed through hematoxylin and eosin (H&E) staining and biochemical index analysis at 5 days after the intravenous injection of the  $^{19}\text{F}$  MRI HNCAs-1 (100  $\mu\text{L}$ ,  $15\text{ mg mL}^{-1}$ ) and PBS (blank) and intratumoral injection of the  $^{19}\text{F}$  MRI HNCAs-1 (50  $\mu\text{L}$ ,  $15\text{ mg mL}^{-1}$ ) and PBS (blank) in to BALB/c mice. The mice were subsequently killed and the major organs, including heart, liver, spleen, lung, and kidney, were collected, and fixed in 4% PFA solution and embedded in paraffin. Embedded tissue specimens were sectioned and photographed by a microscope. Also, 500  $\mu\text{L}$  blood samples from the mice were collected in 1.5 mL centrifuge tubes, followed by centrifugation at 3000 rpm for 10 min at  $4\text{ }^{\circ}\text{C}$ , and the upper serum was collected for biochemical analysis. The serum biochemistry tests included aspartate transaminase (AST), albumin (ALB), total protein (TP), urea (UREA), creatinine (CRE), and cholesterol (CHO). All the experiments concerning the mice samples were approved by the Institutional Animal Care and Use Committee, Sun Yat-sen University (Approval No.: SYSU-IACUC-2020-B1108). We also state that informed consent was obtained for any experimentation with human subjects.

### $^{19}\text{F}$ MRI signal detection inside 4T1 cells

After incubating  $^{19}\text{F}$  MRI HNCAs-1 (concentration:  $10\text{ mg mL}^{-1}$  in DMEM) with 4T1 cells at  $37\text{ }^{\circ}\text{C}$  for 24 h, the 4T1 cells ( $\sim 6 \times$





$10^6$ ) were trypsinized and collected into a 1.5 mL centrifuge tube. Subsequently, the 4T1 cells were centrifuged and washed three times by pure PBS solution. The washed cells were resuspended in 300  $\mu$ L clean DMEM and then subjected to five freeze-thawing cycles. Finally, the cells were centrifuged and the supernatants were collected for  $^{19}\text{F}$  NMR measurement. The cultured DMEM pure solution (the co-culture medium) and the last PBS solution that was used to wash the 4T1 cells were characterized by  $^{19}\text{F}$  NMR.

## Results and discussion

### $^{19}\text{F}$ MRI HNCAs synthesis and characterization

The detailed synthesis procedure and constitution of the  $^{19}\text{F}$  MRI HNCAs are presented in Fig. 1 and the Experimental section. The surfactant-free emulsion co-polymerization of tertiary-butyl acrylate (TBA) and trifluoroethyl methacrylate (TFMA) was applied to synthesize the  $^{19}\text{F}$  MRI HNCAs in this work, because of its simplicity, scale-up potential, and potential for diameter manipulation. TFMA with magnetically equivalent fluorine atoms was chosen as the fluorine marker. By turning the feed ratio of TBA and TFMA during the polymerization, the fluorine content inside the  $^{19}\text{F}$  MRI HNCAs and the  $^{19}\text{F}$  NMR intensity can be easily regulated in principle. During the polymerization, 1% (mole ratio to total monomers) crosslinking agent ((2,2'-dithiodiethanol) diacrylate (2,2'-DED)) (Fig. S6†) was

added to maintain the morphology of the  $^{19}\text{F}$  MRI HNCAs in aqueous solution. In order to verify the validity of this synthesis protocol,  $^{19}\text{F}$  MRI HNCAs-1 with a monomer mole ratio of 9 : 1 (TBA : TFMA = 9 : 1) were first synthesized. Around 30 g polymeric nanoparticles (PNs) (the precursor of the  $^{19}\text{F}$  MRI HNCAs-1) could be prepared by this approach every time.

Fig. 2 presents the dynamic light scattering (DLS) results, showing the PNs-1 with a diameter of  $96 \pm 26$  nm (Fig. 2A, black line). The zeta potential value of PNs-1 was  $-37.7 \pm 0.3$  mV (Fig. 2B, black column) indicating the sufficient negative charge on the surface and their good dispersity in aqueous solution. The TEM image demonstrated the PNs-1 had a spherical structure (Fig. 2C). In order to synthesize the  $^{19}\text{F}$  MRI HNCAs-1, the *tert*-butyl groups inside the PNs-1 were deprotected in the presence of trifluoroacetic acid (TFAA) and formic acid (FA). According to the DLS results (Fig. 2A, red line), the  $^{19}\text{F}$  MRI HNCAs-1 had a diameter of  $230 \pm 73$  nm. The increase in the diameter was caused by the swelling of the hydrophilic poly(acrylic acid)s in the  $^{19}\text{F}$  MRI HNCAs-1. Inside  $^{19}\text{F}$  MRI HNCAs-1, the hydrophilic poly(acrylic acid)s were able to enhance the hydration effect for the nearby fluorine atoms. The zeta potential value of the  $^{19}\text{F}$  MRI HNCAs-1 was  $-22.4 \pm 0.4$  mV, as shown in Fig. 2B (red column), demonstrating that the negative charges ( $\text{SO}_3^{2-}$ ) were not located on surface of the  $^{19}\text{F}$  MRI HNCAs-1, which could be caused by the increased flexibility of the polymer chains and the migration of the negative charges

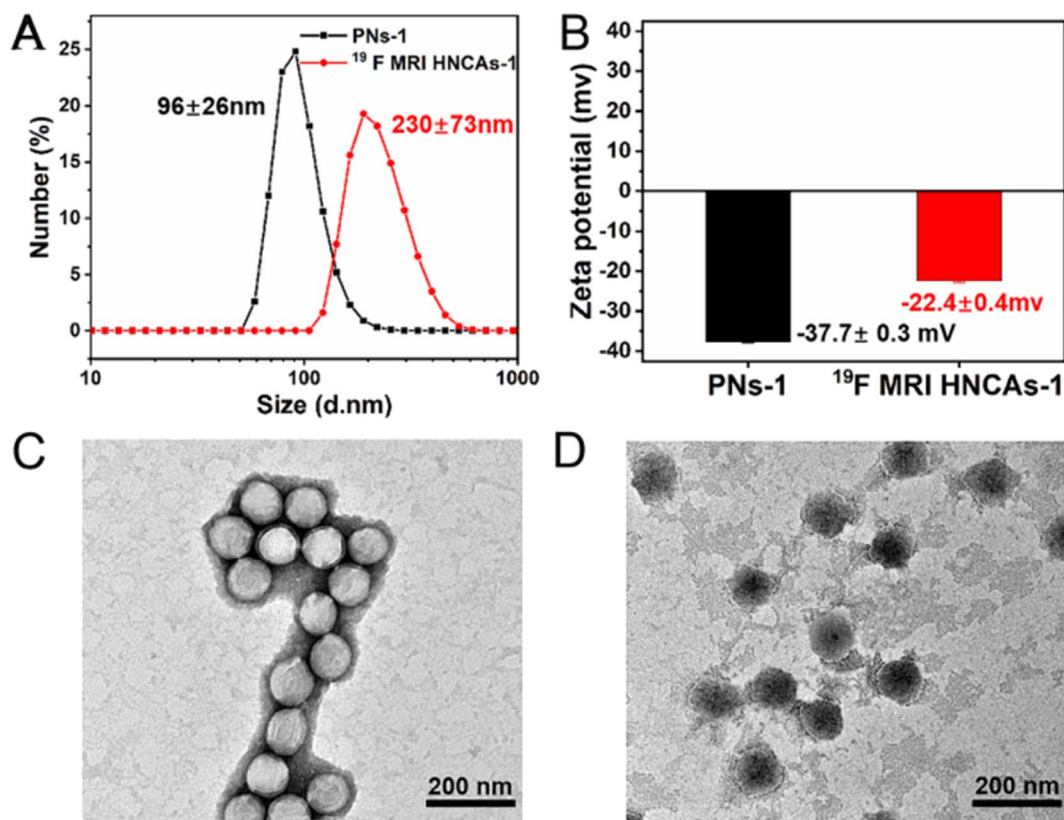


Fig. 2 Structure characterization of PNs-1 and  $^{19}\text{F}$  MRI HNCAs-1. (A) Hydrodynamic diameter values measured by DLS, (B) zeta potential values in  $\text{H}_2\text{O}$ . (C) TEM image of the PNs-1 and (D) TEM image of the  $^{19}\text{F}$  MRI HNCAs-1.

( $\text{SO}_3^{2-}$ ) into the core of the  $^{19}\text{F}$  MRI HNCAs-1. The TEM image in Fig. 2D presented the round morphology of the  $^{19}\text{F}$  MRI HNCAs-1, clearly demonstrating that using 1% crosslinking agent (2,2'-DED) was enough to maintain the integrity of the  $^{19}\text{F}$  MRI HNCAs-1 during the hydrolysis reaction. This is important as nanosized objectives are apt to aggregate in aqueous solution to reduce their total surface energy, especially in the presence of ions. The  $^{19}\text{F}$  MRI HNCAs-1 could maintain their stable hydrodynamic diameter values and PDI for at least 30 days in PBS buffer at room temperature, as shown in Fig. S1,† demonstrating that the  $^{19}\text{F}$  MRI HNCAs-1 could be stored for a long time.

### Magnetic resonance properties of the $^{19}\text{F}$ MRI HNCAs

As discussed in the introduction, the mobility of fluorine atoms is restricted by the hydrophobic interaction among fluorine atoms and *tert*-butyl groups and dipole–dipole interactions among different fluorine atoms in PNs. We hypothesized that the mobility of fluorine atoms in PNs-1 could be optimized by deprotecting the hydrophobic *tert*-butyl groups, and accordingly, the  $^{19}\text{F}$  NMR intensity of the  $^{19}\text{F}$  MRI HNCAs-1 could be promoted, because the left hydrophilic carboxylic groups could enhance the hydration condition around the fluorine atoms. As shown in Fig. 3A, the  $^{19}\text{F}$  NMR intensity of the PNs-1 at a chemical shift of  $-73$  ppm in  $\text{D}_2\text{O}/\text{H}_2\text{O}$  (1/9, v/v) was negligible, while the  $^{19}\text{F}$  NMR intensity (chemical shift of  $-73$  ppm) increased remarkably after removing the *tert*-butyl groups for  $^{19}\text{F}$  MRI HNCAs-1 in  $\text{D}_2\text{O}/\text{H}_2\text{O}$  (1/9, v/v) at the same concentration of nanoobjects ( $10\text{ mg mL}^{-1}$ ). This encouraging result verified our above hypothesis directly. Compared with the  $^1\text{H}$  MRI technology, one of the greatest advantages of  $^{19}\text{F}$  MRI is that the signal intensity is proportional to the fluorine content in  $^{19}\text{F}$  MRI CAs. As shown in Fig. 3B and S2,† the signal-to-noise ratio (SNR) was linearly dependent on the concentration of  $^{19}\text{F}$  MRI HNCAs-1 in aqueous solution ( $2.5\text{--}40\text{ mg mL}^{-1}$ ), indicating the  $^{19}\text{F}$  MRI HNCAs-1 are suitable for quantitative MRI measurements. Because the carboxylic acid groups can undergo protonation and deprotonation when the pH values of the

solution changes, this process may change the hydration environment of fluorine atoms and influence the imaging property of  $^{19}\text{F}$  MRI HNCAs-1. Accordingly,  $^{19}\text{F}$  NMR measurements were also carried out at varying pH values from 3.0 to 11.0. As shown in Fig. S3,† the  $^{19}\text{F}$  signal of  $^{19}\text{F}$  MRI HNCAs-1 maintained a consistent intensity at this pH range, demonstrating the imaging performance of  $^{19}\text{F}$  MRI HNCAs-1 was not influenced by the pH of the surroundings.

Beside the mobility of fluorine atoms, the fluorine content in  $^{19}\text{F}$  MRI CAs also influence the  $^{19}\text{F}$  NMR intensity and the  $^{19}\text{F}$  MRI imaging behavior.<sup>44</sup> Thus, by adjusting the feed mole ratio of monomer TBA and TFMA in the polymerization process, another four  $^{19}\text{F}$  MRI HNCAs samples with different fluorine contents were synthesized by applying the same procedure and conditions as well. Compared with the  $^{19}\text{F}$  MRI HNCAs-1, the fluorine contents of the newly synthesized  $^{19}\text{F}$  MRI HNCAs were enhanced with increasing the feed ratio of TFMA in the polymerization. The detailed monomer ratios and the newly synthesized  $^{19}\text{F}$  MRI HNCAs characteristics are presented in Table S1.† The diameters of the newly synthesized  $^{19}\text{F}$  MRI HNCAs were between 180 nm and 250 nm. As shown in Fig. 4A, before deprotecting the *tert*-butyl groups, the  $^{19}\text{F}$  NMR intensities of the newly synthesized  $^{19}\text{F}$  MRI HNCAs did not appear at a chemical shift of  $-72.9$  ppm, while the  $^{19}\text{F}$  NMR intensities appeared again at a chemical shift of  $-72.9$  ppm after the *tert*-butyl groups were removed, which was consistent with the result of the  $^{19}\text{F}$  MRI HNCAs-1. In principle,  $^{19}\text{F}$  MRI CAs with a higher fluorine content should display a higher  $^{19}\text{F}$  NMR intensity. However, for our  $^{19}\text{F}$  MRI HNCAs,  $^{19}\text{F}$  MRI HNCAs-1, which had the lowest fluorine content, displayed the strongest  $^{19}\text{F}$  NMR intensity at the same fluorine concentration of  $0.7\text{ mg mL}^{-1}$  and aqueous medium volume of  $0.5\text{ mL}$  during the  $^{19}\text{F}$  NMR intensity measurements (Fig. 4A). This could be attributed to the fluorine atoms easily suffering from self-aggregation due to their strong dipole–dipole interactions and super hydrophobicity in aqueous solution. Compared with the other four newly prepared  $^{19}\text{F}$  MRI HNCAs, the low fluorine content inside  $^{19}\text{F}$  MRI HNCAs-1 resulted in the least self-aggregation and the

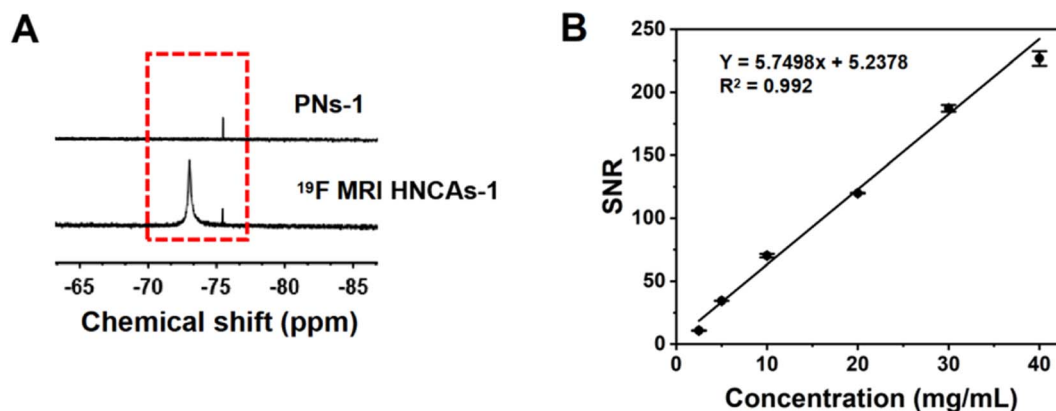


Fig. 3  $^{19}\text{F}$  NMR characterization of  $^{19}\text{F}$  MRI HNCAs-1 in  $\text{D}_2\text{O}/\text{H}_2\text{O}$  (1/9, v/v). (A)  $^{19}\text{F}$  NMR intensity of the PNs-1 and  $^{19}\text{F}$  MRI HNCAs-1 with trifluoroacetate sodium as an internal reference (nano-objects concentration:  $10\text{ mg mL}^{-1}$ ) and (B) SNR values of the  $^{19}\text{F}$  MRI HNCAs-1 at different concentrations ( $2.5\text{--}40\text{ mg mL}^{-1}$ ).



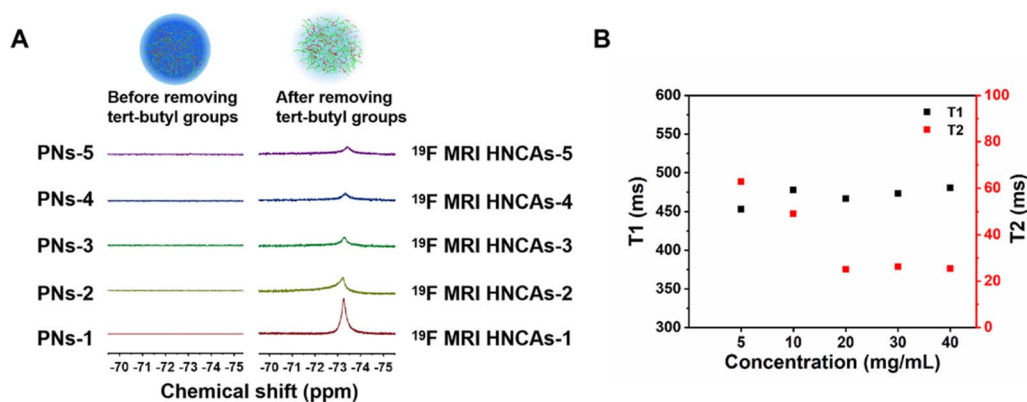


Fig. 4 (A)  $^{19}\text{F}$  NMR intensity of the synthesized PNs and  $^{19}\text{F}$  MRI HNCAs with a fluorine concentration of  $0.7\text{ mg mL}^{-1}$  in  $\text{D}_2\text{O}/\text{H}_2\text{O}$  (1/9, v/v) and (B)  $T_1$  relaxation times and  $T_2$  relaxation times of the  $^{19}\text{F}$  MRI HNCAs-1 at concentrations of 5–40  $\text{mg mL}^{-1}$  in  $\text{D}_2\text{O}/\text{H}_2\text{O}$  (1/9, v/v).

greatest mobility of fluorine atoms, which finally caused it to display the strongest  $^{19}\text{F}$  NMR intensity.

For our research in this article, because  $^{19}\text{F}$  MRI HNCAs-1 had the best  $^{19}\text{F}$  NMR performance in aqueous solution compared with the others, the  $^{19}\text{F}$  MRI HNCAs-1 were chosen for further study. It is well known that calcium ions existing in the cell nutrition medium and bodily fluids *in vivo* can complex with carboxylic acid to form supramolecular crosslinking points,<sup>51</sup> which can slow down the chain segments movement of poly(acrylate acid)s. Because abundant carboxylic acids are located inside the  $^{19}\text{F}$  MRI HNCAs-1, we speculated that the calcium ions probably are able to change the fluorine atoms nearby microstructure and influence the  $^{19}\text{F}$  NMR intensity of the  $^{19}\text{F}$  MRI HNCAs-1. As shown in Fig. S4,<sup>†</sup> the  $^{19}\text{F}$  NMR intensity of the  $^{19}\text{F}$  MRI HNCAs-1 in aqueous solution containing calcium ions with a concentration of  $6\text{ mg mL}^{-1}$  was almost the same with that in a calcium ions-free aqueous solution, which demonstrated that the formation of supramolecular crosslinking points between carboxylic acids and calcium ions surrounding fluorine atoms could not prohibit the mobilities of the fluorine atoms and decrease the  $^{19}\text{F}$  NMR intensity of the  $^{19}\text{F}$  MRI HNCAs-1.

In aqueous solution, a longer  $T_2$  relaxation time of  $^{19}\text{F}$  MRI CAs is essential for generating high-resolution  $^{19}\text{F}$  MRI images *in vitro* and *in vivo*. Normally, an ideal  $^{19}\text{F}$  MRI CA should have a  $T_2$  relaxation time longer than 10 ms for achieving excellent performance in *in vivo* imaging.<sup>27</sup> Therefore, the  $T_1$  and  $T_2$  relaxation times of the  $^{19}\text{F}$  MRI HNCAs-1 were measured using the inversion-recovery and Carr–Purcell–Meiboom–Gill (CPMG) pulse sequences, respectively. The  $T_2$  relaxation time of  $^{19}\text{F}$  MRI HNCAs-1 at concentrations from  $5\text{ mg mL}^{-1}$  to  $10\text{ mg mL}^{-1}$  were all over 40 ms without drastic change, indicating that the fluorine atoms maintained their constant mobility in this concentration range, as shown in Fig. 4B. The  $T_2$  relaxation time longer than 10 ms for  $^{19}\text{F}$  MRI HNCAs-1 was attributed to the good mobility of fluorine atoms inside the hydration microenvironment caused by the nearby hydrophilic carboxyl groups. However, the  $T_2$  relaxation time decreased to around 25 ms when the concentration of the  $^{19}\text{F}$  MRI HNCAs-1 increased to

$20\text{ mg mL}^{-1}$ , while the  $T_2$  relaxation times of around 25 ms were stably maintained in the concentration range of 20–40  $\text{mg mL}^{-1}$ . Obviously,  $^{19}\text{F}$  MRI HNCAs-1 had  $T_2$  relaxation times longer than 10 ms in the concentration range of 5–40  $\text{mg mL}^{-1}$ , demonstrating the  $^{19}\text{F}$  MRI HNCAs-1 have great potential for use in imaging. The  $T_1$  relaxation times of  $^{19}\text{F}$  MRI HNCAs-1 in the concentration range of 5–40  $\text{mg mL}^{-1}$  were maintained as 450–500 ms without any obvious concentration dependency.

#### $^{19}\text{F}$ MRI imaging behavior of the $^{19}\text{F}$ MRI HNCAs-1 *in vitro*

As discussed above, the  $^{19}\text{F}$  MRI HNCAs-1 displayed an excellent  $^{19}\text{F}$  NMR intensity and long  $T_2$  relaxation time in aqueous solution as shown in Fig. 4, thus the  $^{19}\text{F}$  MRI HNCAs-1 should be able to perform well in  $^{19}\text{F}$  MRI *in vitro* in principle. As shown in Fig. 5, hot-spot images of the  $^{19}\text{F}$  MRI HNCAs-1 aqueous solution at concentrations of 5–40  $\text{mg mL}^{-1}$  were successfully obtained. Moreover, the brightness of the hot-spot images was linearly dependent on the concentration of the  $^{19}\text{F}$  MRI HNCAs-1. In comparison, the aqueous solution of the PNs-1 (before deprotecting the *tert* groups) did not show an  $^{19}\text{F}$  MRI intensity in the same concentration range and measuring condition. The *in vitro* hot-spot imaging results were agreement with the  $^{19}\text{F}$  NMR outcome in Fig. 3A, showing that removing the hydrophobic *tert*-butyl groups was able to endow the  $^{19}\text{F}$  MRI HNCAs-1 with a strong fluorine atoms mobility and  $^{19}\text{F}$  NMR intensity.

#### Cell-uptake behavior and biocompatibility of the $^{19}\text{F}$ MRI HNCAs-1

The successful imaging behaviors of the  $^{19}\text{F}$  MRI HNCAs-1 aqueous solution *in vitro* encouraged us to explore their application potential at the cellular level. The cell-uptake behavior of the  $^{19}\text{F}$  MRI HNCAs-1 was first investigated by flow cytometry in both red and green channels. In order to trace the  $^{19}\text{F}$  MRI HNCAs-1 by flow cytometry, the  $^{19}\text{F}$  MRI HNCAs-1 were first modified by rhodamine-123 with EDC·HCl and NHS. As shown in Fig. S5,<sup>†</sup> the fluorescence emission at 530 nm in the fluorescence spectrum demonstrated the successful modification of rhodamine-123 on the  $^{19}\text{F}$  MRI HNCAs-1. As shown in Fig. 6A, at 1 h post incubation of the  $^{19}\text{F}$  MRI HNCAs-1 with 4T1 cells

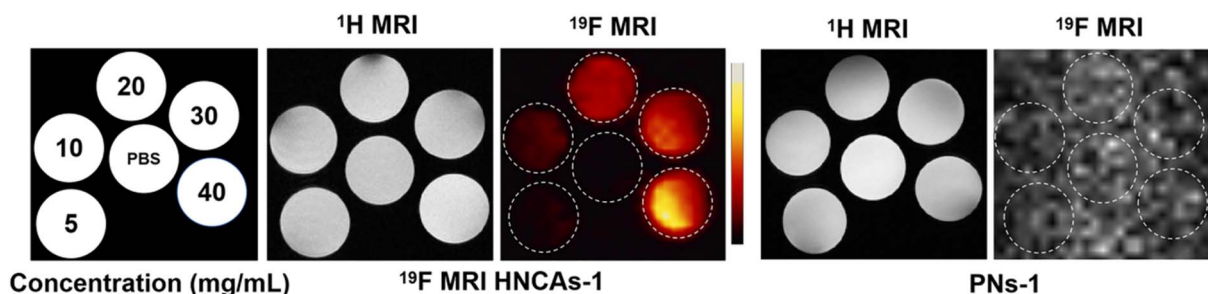


Fig. 5  $^1\text{H}/^{19}\text{F}$  MRI performances of the  $^{19}\text{F}$  MRI HNCAs-1 and PNs-1 aqueous solution at concentrations of 5–40  $\text{mg mL}^{-1}$  *in vitro*.

(breast cancer cell), the fluorescence histograms demonstrated that the  $^{19}\text{F}$  MRI HNCAs-1 had been endocytosed by 4T1 already. The fast uptake behavior of the  $^{19}\text{F}$  MRI HNCAs-1 by 4T1 cells could probably be attributed to the extreme hydrophilicity of the carboxylic acid groups located on the surface of the  $^{19}\text{F}$  MRI HNCAs-1. The uptake amount of the  $^{19}\text{F}$  MRI HNCAs-1 by 4T1 cells reached a maximum at 4 h post incubation. After that, the amount of  $^{19}\text{F}$  MRI HNCAs-1 inside the 4T1 cells started to decrease due to the metabolism process inside the 4T1 cells. The mean fluorescence intensities of the 4T1 cell exploration outcomes were in agreement with the above fluorescence histograms results, as shown in Fig. 6B. In addition, in order to confirm the cell-uptake behavior, CLSM was used to visualize the presence of rhodamine-123-modified  $^{19}\text{F}$  MRI HNCAs-1

inside the 4T1 cells. As shown in Fig. 6C, the Z-slices through the cellular equator presented obvious blue and green fluorescence signals, largely within the cytoplasm of the 4T1 cancer cells, demonstrating the successful cellular uptake at 4 h post incubation of the  $^{19}\text{F}$  MRI HNCAs-1 with 4T1 cells. The successful uptake behavior demonstrated that the  $^{19}\text{F}$  MRI HNCAs-1 hold potential in imaging species and metabolic processes inside cells.

As practicable  $^{19}\text{F}$  MRI CAs, the biocompatibility and toxicity of the  $^{19}\text{F}$  MRI HNCAs-1 for cells and mice are determining factors. The cytotoxicity of the  $^{19}\text{F}$  MRI HNCAs-1 was first investigated against 4T1 cells and HUVEC (human umbilical vein endothelial cells) by 3-(4,5-dimethylthiazol-2-yl)-2,5-diphenyltetrazolium bromide (MTT) assays. As shown in

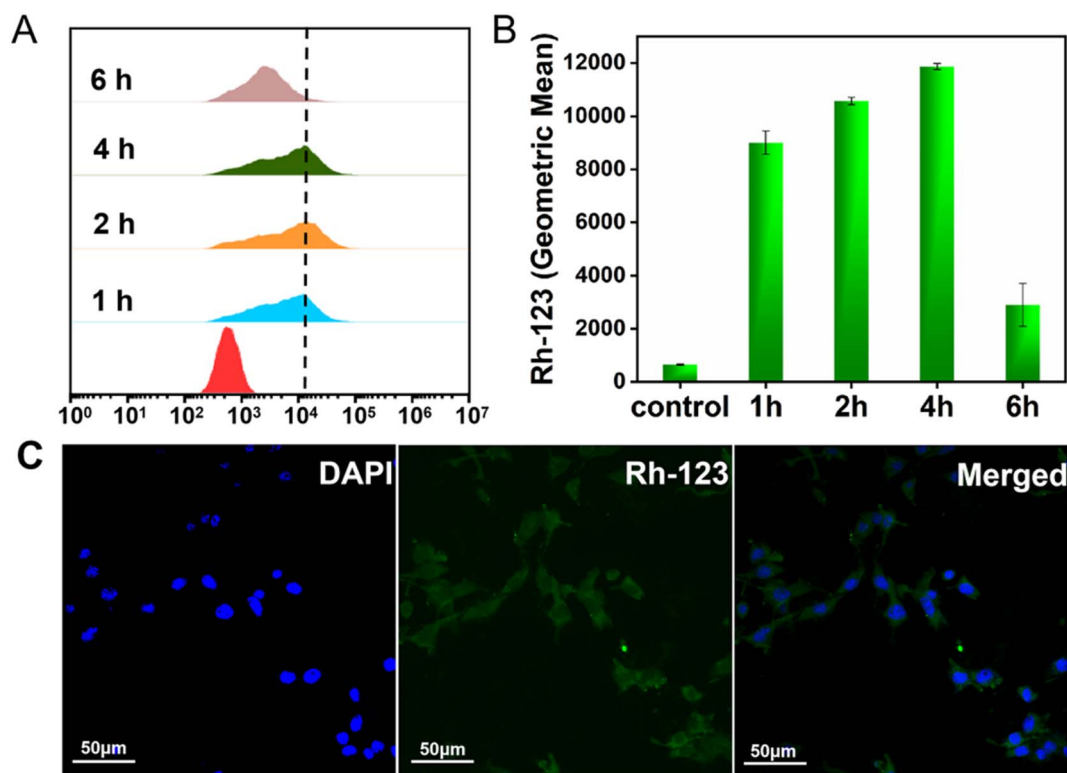


Fig. 6  $^{19}\text{F}$  MRI HNCAs-1 cell-uptake-behavior characterization. (A). Fluorescence histograms of the 4T1 cells after incubation with  $^{19}\text{F}$  MRI HNCAs-1 at incubation times of 1–6 h, (B) mean fluorescence intensities of the 4T1 cells after incubation with  $^{19}\text{F}$  MRI HNCAs-1 at incubation times of 1–6 h, (C) CLSM images of the uptake behavior of  $^{19}\text{F}$  MRI HNCAs-1 inside 4T1 cells.





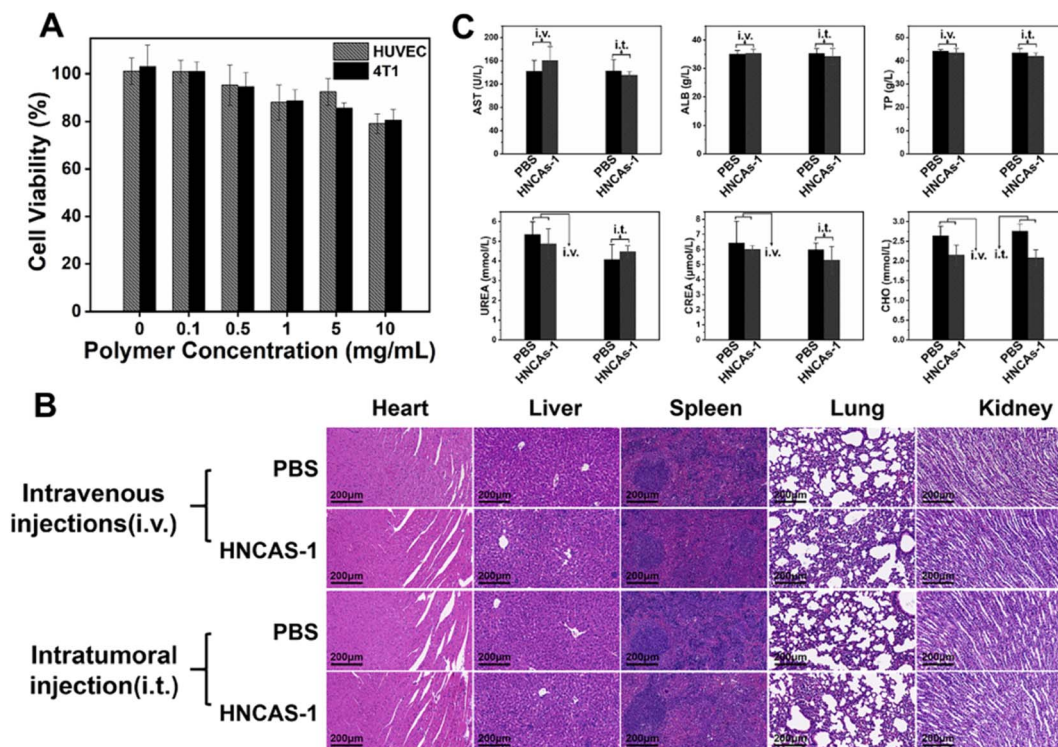


Fig. 7 Biosafety results of the  $^{19}\text{F}$  MRI HNCAs-1. (A) Cells viabilities against 4T1 and HUVEC cells, (B) H&E staining images of the main organs of mice at 5 days post administrating the  $^{19}\text{F}$  MRI HNCAs-1, (C) physiology indices values of the mice at 5 days post administrating the  $^{19}\text{F}$  MRI HNCAs-1.

Fig. 7A, the  $^{19}\text{F}$  MRI HNCAs-1 at concentrations of 0.1 to 10  $\text{mg mL}^{-1}$  showed cell viability ratios above 80% after 24 h incubation, demonstrating the  $^{19}\text{F}$  MRI HNCAs-1 had excellent

biocompatibility for both cancer and mammalian cells. In order to systematically access the biocompatibility and safety in mice, 100  $\mu\text{L}$   $^{19}\text{F}$  MRI HNCAs-1 with a concentration of 15  $\text{mg mL}^{-1}$

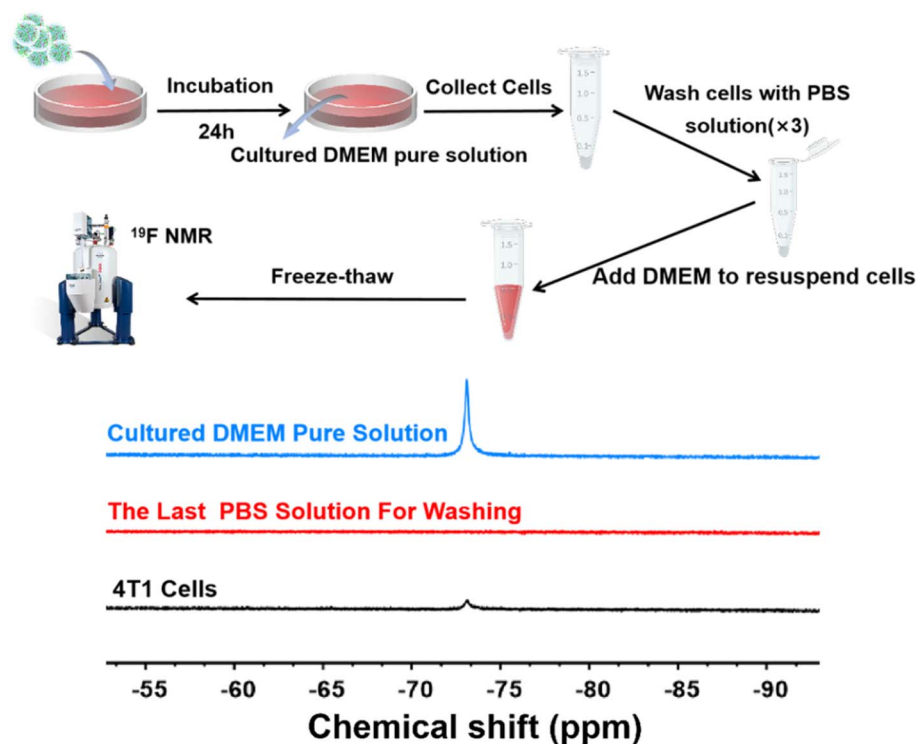


Fig. 8  $^{19}\text{F}$  NMR intensity of  $^{19}\text{F}$  MRI HNCAs-1 within 4T1 cells.

was administrated into mice *via* lateral tail vein injection and intratumoral injection. At 5 days post-injection of the  $^{19}\text{F}$  MRI HNCAs-1, the important organs (heart, liver, spleen, lung, and kidney) of the mice were harvested and subjected to histological examination. The H&E staining images of the main organs indicated that they maintained their typical physiological structures without any tissue damage, as shown in Fig. 7B. In addition, the main physiology indices of blood, including albumin (ALB), aspartate transaminase (AST), creatinine (CRE), total protein (TP), cholesterol (CHOL), and urea (UREA), were at similar levels to the PBS control group, both maintaining a healthy level, as shown in Fig. 7C. All the above exploration results demonstrated that the  $^{19}\text{F}$  MRI HNCAs-1 possess satisfactory biosafety.

### $^{19}\text{F}$ MRI capability of the $^{19}\text{F}$ MRI HNCAs-1 inside 4T1 cells

The  $^{19}\text{F}$  MRI HNCAs-1 displayed excellent  $^{19}\text{F}$  NMR intensity,  $^{19}\text{F}$  MRI performance *in vitro*, highly efficient cell-uptake behavior, and excellent biosafety against cells and mice. As a result, we hypothesized that the  $^{19}\text{F}$  MRI HNCAs-1 would be able to image inside cells. To test this hypothesis, the  $^{19}\text{F}$  MRI HNCAs-1 were co-cultured with 4T1 cells for 24 h. The detailed purification processes are shown in Fig. 8 and described in the Experimental section. As shown in Fig. 8, the cultured DMEM pure solution showed  $^{19}\text{F}$  NMR intensity (blue line) demonstrating that not all the  $^{19}\text{F}$  MRI HNCAs-1 could be phagocytosed by 4T1 cells during the co-culture. In order to confirm that the  $^{19}\text{F}$  MRI HNCAs-1 could image inside 4T1 cells after being phagocytosed, the co-cultured 4T1 cells were carefully washed with PBS three times to wash away any free  $^{19}\text{F}$  MRI HNCAs-1 outside the 4T1 cells. The  $^{19}\text{F}$  NMR signal at a chemical shift of  $-73$  ppm of the PBS washing solution (the third-time of washing solution) was not detectable (red line), demonstrating the free  $^{19}\text{F}$  MRI HNCAs-1 outside the 4T1 cells had been fully washed away. After the freeze–thawing processes, the remaining 4T1 cells were transferred and characterized by  $^{19}\text{F}$  NMR in DMEM. The appearance of the  $^{19}\text{F}$  NMR signal at a chemical shift of  $-73$  ppm (black line) indicated that the  $^{19}\text{F}$  MRI HNCAs-1 inside 4T1 cells still maintained their  $^{19}\text{F}$  MRI capability. The above results demonstrated again that the  $^{19}\text{F}$  MRI HNCAs-1 could be endocytosed by 4T1 cells. More importantly, the  $^{19}\text{F}$  NMR intensity of the endocytosed  $^{19}\text{F}$  HNCAs-1 inside 4T1 was still retained.

## Conclusion

We developed a simple and high-performance surfactant-free emulsion polymerization strategy to synthesize  $^{19}\text{F}$  MRI CAs utilizing commercial fluorinated monomers. The research results demonstrated that donating a good hydration micro-environment surrounding the fluorine atoms could promote the mobility of the fluorine atoms and enhance the  $^{19}\text{F}$  MR imaging performance of the  $^{19}\text{F}$  MRI CAs. However, an intensive  $^{19}\text{F}$  NMR intensity could not be achieved by just increasing the amount of fluorinated monomer during the synthesis process or the fluorine content in the  $^{19}\text{F}$  MRI HNCAs. The  $^{19}\text{F}$  MRI HNCAs-1 displayed long-term storage stability, robust

functional stability, great biosafety *in vivo*, and excellent  $^{19}\text{F}$  MR imaging capability *in vitro*. For that reason, we believe that the  $^{19}\text{F}$  MRI HNCAs-1 could serve as a powerful  $^{19}\text{F}$  MRI contrast agent for not only the precise imaging of lesion sites (such as tumor, inflammation) but also could be used for cell tracking *in vivo* non-invasively. Additionally, the strategy used to prepare the  $^{19}\text{F}$  MRI CAs in this article has a certain referential significance for the preparation of new types of  $^{19}\text{F}$  MRI CAs.

## Conflicts of interest

The authors declare they have no competing financial interests.

## Acknowledgements

Dalin Wu acknowledges the financial support of the National Natural Science Foundation of China (22075327) and the Natural Science Foundation of Guangdong Province (2022A1515011392). In addition, Zheng Hu was acknowledged for her constructive suggestion on running the cell experiments.

## References

- 1 P. Debbage and W. Jaschke, *Histochem. Cell Biol.*, 2008, **130**, 845–875.
- 2 E. T. Ahrens and J. W. M. Bulte, *Nat. Rev. Immunol.*, 2013, **13**, 755–763.
- 3 J. Wahsner, E. M. Gale, A. Rodríguez-Rodríguez and P. Caravan, *Chem. Rev.*, 2019, **119**, 957–1057.
- 4 D. Hao, T. Ai, F. Goerner, X. Hu, V. M. Runge and M. Tweedle, *J. Magn. Reson. Imaging*, 2012, **36**, 1060–1071.
- 5 J. L. Major and T. J. Meade, *Acc. Chem. Res.*, 2009, **42**, 893–903.
- 6 P. Caravan, J. J. Ellison, T. J. McMurphy and R. B. Lauffer, *Chem. Rev.*, 1999, **99**, 2293–2352.
- 7 H. B. Na, I. C. Song and T. Hyeon, *Adv. Mater.*, 2009, **21**, 2133–2148.
- 8 M.-F. Bellin, *Eur. J. Radiol.*, 2006, **60**, 314–323.
- 9 J. T. Heverhagen, G. A. Krombach and E. Gizewski, *Rofo*, 2014, **186**, 661–669.
- 10 P. S. N. Rowe, L. V. Zelenchuk, J. S. Laurence, P. Lee, W. M. Brooks and E. T. McCarthy, *Am. J. Physiol.*, 2015, **309**, F764–F769.
- 11 J. C. Knight, P. G. Edwards and S. J. Paisey, *RSC Adv.*, 2011, **1**, 1415–1425.
- 12 E. T. Ahrens, B. M. Helfer, C. F. O'Hanlon and C. Schirda, *Magn. Reson. Med.*, 2014, **72**, 1696–1701.
- 13 A. Mali, E. L. Kaijzel, H. J. Lamb and L. J. Cruz, *J. Controlled Release*, 2021, **338**, 870–889.
- 14 E. T. Ahrens and J. Zhong, *NMR Biomed.*, 2013, **26**, 860–871.
- 15 E. T. Ahrens, R. Flores, H. Xu and P. A. Morel, *Nat. Biotechnol.*, 2005, **23**, 983–987.
- 16 M. Srinivas, P. A. Morel, L. A. Ernst, D. H. Laidlaw and E. T. Ahrens, *Magn. Reson. Med.*, 2007, **58**, 725–734.
- 17 J.-X. Yu, R. R. Hallac, S. Chiguru and R. P. Mason, *Prog. Nucl. Magn. Reson. Spectrosc.*, 2013, **70**, 25–49.



- 18 G. D. Kenny, K. P. Shaw, S. Sivachelvam, A. J. P. White, R. M. Botnar and R. T. M. de Rosales, *J. Fluorine Chem.*, 2016, **184**, 58–64.
- 19 J. Zhang, Y. Yuan, Y. Li, H. Yang, H. Zhang, S. Chen, X. Zhou, Z. Yang and Z.-X. Jiang, *J. Org. Chem.*, 2020, **85**, 6778–6787.
- 20 Z.-X. Jiang and Y. B. Yu, *J. Org. Chem.*, 2010, **75**, 2044–2049.
- 21 M. Ogawa, S. Nitahara, H. Aoki, S. Ito, M. Narazaki and T. Matsuda, *Macromol. Chem. Phys.*, 2010, **211**, 1602–1609.
- 22 J. Ruiz-Cabello, B. P. Barnett, P. A. Bottomley and J. W. M. Bulte, *NMR Biomed.*, 2011, **24**, 114–129.
- 23 I. Tirotta, V. Dichiarante, C. Pigliacelli, G. Cavallo, G. Terraneo, F. B. Bombelli, P. Metrangolo and G. Resnati, *Chem. Rev.*, 2015, **115**, 1106–1129.
- 24 R. Holman, O. Lorton, P. C. Guillemain, S. Desgranges, C. Contino-Pépin and R. Salomir, *Front. Chem.*, 2022, **9**, 810029.
- 25 I. N. Kuznetsova, *Pharmaceutical Chemistry Journal*, 2003, **37**, 415–420.
- 26 Y. Huang, A. M. Vezeridis, J. Wang, Z. Wang, M. Thompson, R. F. Mattrey and N. C. Gianneschi, *J. Am. Chem. Soc.*, 2017, **139**, 15–18.
- 27 D. Jirak, A. Galisova, K. Kolouchova, D. Babuka and M. Hruby, *Magn. Reson. Mater. Phys., Biol. Med.*, 2019, **32**, 173–185.
- 28 Y. Wang, X. Tan, A. Usman, Y. Zhang, M. Sawczyk, P. Král, C. Zhang and A. K. Whittaker, *ACS Macro Lett.*, 2022, **11**, 1195–1201.
- 29 K. J. Thurecht, I. Blakey, H. Peng, O. Squires, S. Hsu, C. Alexander and A. K. Whittaker, *J. Am. Chem. Soc.*, 2010, **132**, 5336–5337.
- 30 B. E. Rolfe, I. Blakey, O. Squires, H. Peng, N. R. B. Boase, C. Alexander, P. G. Parsons, G. M. Boyle, A. K. Whittaker and K. J. Thurecht, *J. Am. Chem. Soc.*, 2014, **136**, 2413–2419.
- 31 Z. Guo, M. Gao, M. Song, Y. Li, D. Zhang, D. Xu, L. You, L. Wang, R. Zhuang, X. Su, T. Liu, J. Du and X. Zhang, *Adv. Mater.*, 2016, **28**, 5898–5906.
- 32 Y. Yuan, S. Ge, H. Sun, X. Dong, H. Zhao, L. An, J. Zhang, J. Wang, B. Hu and G. Liang, *ACS Nano*, 2015, **9**, 5117–5124.
- 33 H. Lin, X. Tang, A. Li and J. Gao, *Adv. Mater.*, 2021, **33**, 2005657.
- 34 C. Fu, B. Demir, S. Alcantara, V. Kumar, F. Han, H. G. Kelly, X. Tan, Y. Yu, W. Xu, J. Zhao, C. Zhang, H. Peng, C. Boyer, T. M. Woodruff, S. J. Kent, D. J. Searles and A. K. Whittaker, *Angew. Chem., Int. Ed.*, 2020, **59**, 4729–4735.
- 35 X. Zhu, X. Tang, H. Lin, S. Shi, H. Xiong, Q. Zhou, A. Li, Q. Wang, X. Chen and J. Gao, *Chem*, 2020, **6**, 1134–1148.
- 36 K. L. Peterson, K. Srivastava and V. C. Pierre, *Front. Chem.*, 2018, **6**, 160–181.
- 37 C. Zhang, Y. Zhou, Q. Liu, S. Li, S. Perrier and Y. Zhao, *Macromolecules*, 2011, **44**, 2034–2049.
- 38 K. Wang, H. Peng, K. J. Thurecht, S. Puttick and A. K. Whittaker, *Polym. Chem.*, 2014, **5**, 1760–1771.
- 39 K. Wang, H. Peng, K. J. Thurecht, S. Puttick and A. K. Whittaker, *Biomacromolecules*, 2015, **16**, 2827–2839.
- 40 S. Li, J. Han and C. Gao, *Polym. Chem.*, 2013, **4**, 1774–1787.
- 41 O. Munkhbat, M. Canakci, S. Zheng, W. Hu, B. Osborne, A. A. Bogdanov and S. Thayumanavan, *Biomacromolecules*, 2019, **20**, 790–800.
- 42 N. J. Warren and S. P. Armes, *J. Am. Chem. Soc.*, 2014, **136**, 10174–10185.
- 43 X. Tang, X. Gong, A. Li, H. Lin, C. Peng, X. Zhang, X. Chen and J. Gao, *Nano Lett.*, 2020, **20**, 363–371.
- 44 Y. Mo, C. Huang, C. Liu, Z. Duan, J. Liu and D. Wu, *Macromol. Rapid Commun.*, 2023, 2200744.
- 45 D. Janasik and T. Krawczyk, *Chem. - Eur. J.*, 2022, **28**, e202102556.
- 46 W. Zhao, H. T. Ta, C. Zhang and A. K. Whittaker, *Biomacromolecules*, 2017, **18**, 1145–1156.
- 47 C. Zhang, S. S. Moonshi, Y. Han, S. Puttick, H. Peng, B. J. A. Magoling, J. C. Reid, S. Bernardi, D. J. Searles, P. Král and A. K. Whittaker, *Macromolecules*, 2017, **50**, 5953–5963.
- 48 C. Zhang, S. S. Moonshi, W. Wang, H. T. Ta, Y. Han, F. Y. Han, H. Peng, P. Král, B. E. Rolfe, J. J. Gooding, K. Gaus and A. K. Whittaker, *ACS Nano*, 2018, **12**, 9162–9176.
- 49 X. Tang, A. Li, C. Zuo, X. Liu, X. Luo, L. Chen, L. Li, H. Lin and J. Gao, *ACS Nano*, 2023, **17**, 5014–5024.
- 50 C. Miao, F. Li, Y. Zuo, R. Wang and Y. Xiong, *RSC Adv.*, 2016, **6**, 3013–3019.
- 51 M. B. Gindele, K. K. Malaszuk, C. Peter and D. Gebauer, *Langmuir*, 2022, **38**, 14409–14421.

